Journal of Theoretical and Computational Acoustics

Applicability of 3D Spectral Element Method for Computing Close-Range Underwater Piling Noises

C. Jeong[*,a], A. Manalaysay[a], H. N. Gharti[c], S. Guan[b], and J. Vignola[b]

[a] *Department of Civil and Environmental Engineering*
[b] *Department of Mechanical Engineering*
The Catholic University of America, Washington, DC 20064, USA
[c] *Department of Geosciences*
Princeton University, NJ 08544, USA

Pile driving is used for constructing foundation supports for offshore structures. Underwater noise, induced by in-water pile driving, could adversely impact marine life near the piling location. Many studies have computed this noise in close ranges by using semi-analytical models and Finite Element Method (FEM) models. This work presents a Spectral Element Method (SEM) wave simulator as an alternative simulation tool to obtain close-range underwater piling noise in complex, fully three-dimensional, axially-asymmetric settings in the time domain for impacting force signals with high-frequency contents (e.g., frequencies greater than 1000 Hz).

The presented numerical results show that the flexibility of SEM can accommodate the axially-asymmetric geometry of a model, its heterogeneity, and fluid-solid coupling. We showed that there are multiple Mach Cones of different angles in fluid and sediment caused by the differences of waves' speeds in fluid, a pile, and sediment. The angles of Mach Cones in our numerical results match those that are theoretically evaluated. A previous work [1] had shown that Mach Cone waves lead to intense amplitudes of underwater piling noise via a FEM simulation in an axis-symmetric setting. Whereas it modeled sediment as fluid with a larger wave speed than that of water, we examined if our SEM simulation, using solid sediment-fluid coupling, leads to additional Mach Cones. Because this work computes the shear wave in sediment and the downward-propagating shear wave in a pile, we present six Mach Cones in fluid and sediment induced by downward-propagating P- and S-waves in a pile in lieu of two previously-reported Mach Cones in fluid and sediment (modeled as fluid) induced by a downward-propagating P-wave in a pile. We also showed that the amplitudes of the close-range underwater noise are dependent on the cross-sectional geometry of a pile. In addition, when a pile is surrounded by a solid of an axially-asymmetric geometry, waves are reflected from the surface of the surrounding solid back to the fluid so that constructive and destructive interferences of waves take place in the fluid and affect the amplitude of the underwater piling noise.

Keywords: Spectral element method; Close-range underwater piling noises; and Axially-asymmetric settings

1. Introduction

In-water pile driving methodology has been widely used in foundation construction of offshore wind turbines, bridges, offshore oil and gas platforms, and various coastal structures, such as ferry terminals, docks, and piers. In particular, there has been a large increase in recent years on pile driving activities of offshore wind turbines due to increasing demand for

[*]Corresponding author: jeong@cua.edu

renewable energy [2]. According to the 2015 report of National Renewable Energy Laboratory (NREL), the global offshore wind market is growing such that more than 47,000 MW of global offshore wind capacity is set to be commissioned by 2020 [3] while the turbines themselves are increasing in power output up to several MW each. Continuous global economic growth leads to unceasing needs to build transportation systems, such as bridges and ferry terminals. Moreover, the increasing population also leads to increasing demand for oil and natural gas so that the construction of offshore oil platforms have grown in large numbers [4].

Offshore piling methods involve driving piles, usually made of metals, down into the seabed by means of hammering. Offshore piling poses a potential threat to marine life because in-water pile driving produces intense, broadband (20 Hz to 20 kHz) underwater acoustic noises [5–7]. Underwater piling noises are known to be harmful to fish near a piling location [7,8]. Other environmental consequences include various adverse auditory and behavioral effects to many marine species including marine mammals. For example, intense noise from pile driving has been shown to cause a temporary shift of hearing threshold to harbor porpoise at close ranges [9]. Even at a distance that is considered safe in terms of the hearing-threshold shift, noise levels from pile driving are still at high levels [10, 11] and could induce behavioral disturbances to marine mammals [12]. Furthermore, the increase in background sound levels and the shift of soundscape dynamics, from piling noise, could also lead to acoustic masking in marine mammals [12]. Therefore, in order to accurately assess the environmental impacts of in-water pile driving to marine habitat and mitigate them, it is crucial to understand the noise generated from piling activities. As suggested by Nedwell et al. [5], a reliable, robust and accurate method of computing underwater piling noise and assessing its environmental impact is of importance in providing an optimal design or process for offshore piling construction. Tsouvalas and Metrikine [13] suggested that the noise generation mechanisms in a system that consists of a pile, soil and water must be understood before any noise mitigation efforts take place.

There have been a number of research studies that use analytical (i.e., using closed-form solutions) or semi-analytical methods to calculate underwater noise. For example, Tsouvalas and Metrikine [13–17] presented a three-dimensional semi-analytical model that is proven to be fast, computationally inexpensive, and flexible enough to accommodate the complexity of pile-water-soil interaction during offshore piling. Their model consists of a pile, which is a shell-type structure, surrounded by a layered three-dimensional acousto-elastic domain [16]. They use a linear high-order shell theory for solving the shell's dynamics. The fluid domain was modeled to be an inviscid compressible medium while the soil domain was simplified to be an assemblage of springs and dashpots [16], representing the dynamic stiffness and damping of underlying seabed [18]. The modal decomposition method is applied to solve the dynamic response of each system considering the kinematic interface relationship of each domain [15]. They confirmed conical fronts of acoustic waves, which were first recognized by Reinhall and Dahl [1], as the primary behavior of the waves in the surrounding fluid. They also found that pile driving generates Scholte waves in the seabed-water interface [15]. Dahl and Dall'Osto [19] modeled the radial expansion of sounds from a vertical line array of discrete sound sources along a pile. Each source is given a complex-valued, depth-dependent phase delay compared to its neighbors, and the sound in water in the frequency domain due to each source is calculated by using the Green's function. The frequency-domain sounds are converted into a time signal at the location of a receiver. They also validated their computational modeling with measured data during a real piling site. In their study, the key features in the numerically-predicted sound signals approximately match those of the measured signals at receivers.

Additionally, a number of studies have used the Finite Element Method (FEM) to examine the physical behavior of in-water piling noise. FEM can accommodate realistic, complex environments and thus provides a more accurate underwater piling noise than the aforementioned analytical methods despite its expensive computational cost associated with a dense discretization of a domain. Reinhall and Dahl [1] used the FEM and showed that underwater piling noises stem primarily from a radially-expanding Mach wave from the pile. They used a commercial FEM software (Comsol Multiphysics) to study the dynamic behavior of an axially-symmetric FEM model of a pile. However, the sediment in their study was modeled as fluid. In acknowledging this limitation, they suggest a more accurate elastic description of sediment that includes shear deformation and plasticity will be needed. On the other hand, Heitmann et al. [20] developed a finite element pile driving model, which uses an elasto-plastic soil model that takes into account the plastic deformation of sediment. Their numerical results are validated using data from a measurement campaign done in the German North Sea. Lippert et al. [21] used an axially-symmetric FEM model to characterize the close-range noise generated during offshore piling. Their close-range results are in good agreement with field measurement data. They also devised an alternative approach for analyzing the far-range characteristics of underwater noise using wave number integration. They argued that using an FEM model in determining long-range propagation of underwater sound is not practically feasible due to large computational cost. Fricke and Rolfes [22] used an approach, which integrates three sub-models in predicting underwater noise from offshore piling. The first sub-model uses a linear, axially-symmetric, frequency-domain FEM solver to examine the radiation of pile vibrations to the surrounding water and soil column. The second sub-model uses an analytical approach to determine the mechanical excitation of the pile. The third sub-model, based on a split-step Padé solution of the parabolic equation, is used to define the long-range propagation of the resulting sound in water. Although this model tends to underestimate the sound pressure level at low frequencies, their model showed reasonably accurate results and is suitable for long-range quantitative prediction of underwater noise up to 1500 m. Recently, an international workshop, so-called 'COMPILE (a portmanteau combining computation, comparison, and pile)', was held to compare the results of different numerical models for computing the underwater piling noise of a benchmark model problem in 2016 [23]. The workshop was intended to address the absence of any analytical solution for the problem and the shortage of available measurement data. Seven different teams from six countries attended the workshop. The benchmark problem of the workshop considers a generic thin-walled pile, subject to a force function on its top surface. The lower part of the pile is embedded into the sediment. They consider the sediment as fluid (i.e., the shear waves of the sediment were neglected). The attenuation in fluid and sediment were considered. Most of the presented numerical models in the workshop split the underwater piling noises into close-range and far-range models in order to reduce the computational costs. To couple their close-range numerical solution with the far-range solutions, they used wavenumber integration or parabolic equation approximation method or normal mode expansion. Among the seven numerical models for computing the close-range numerical solution, six of them are the FEM models, and the remaining one is the Finite Difference Method (FDM) model. Five of the FEM models used commercial software (e.g., Comsol and Abaqus) and the other model used the PAFEC-FE software suite. The FEM models used the axially-symmetric 3D setting, which is not a fully 3D one. All the six FEM models produced similar waveforms at a close range up to a distance of 31 m from the pile, whereas the FDM model results in a wave signal that is substantially different from the FEM solutions.

We note that all the numerical models for the close-range noise discussed in our literature review are limited to the axially-symmetric models that are not full 3D, and many of them have simplified sediment as fluid. Thus, we are interested in using the axially-asymmetric, full-3D models for computing close-range underwater piling noises by considering detailed boundary conditions. To this end, we explore a powerful simulation tool to obtain underwater piling noise in the complex, axially-asymmetric domain and in the high-frequency range (e.g., >1000 Hz). While several numerical techniques (for instance, FDM, Boundary Element Method (BEM), and classical low-order FEM) can be employed to solve the full wave equation in complex underwater configurations, Spectral Element Method (SEM) is known to be the most effective and efficient for solving 3D time-domain wave propagation analysis problems of a very large number of meshes and time steps without compromising accuracy [24]. The SEM is a higher-order FEM that uses a nodal quadrature, namely the Gauss-Legendre-Lobatto (GLL) quadrature, leading to a diagonal mass matrix without using mass lumping. Thus, very fast explicit time integration can be used, taking full advantage of a diagonal mass matrix, without compromising accuracy and scalability. An open-source large-scale parallel SEM wave simulator, SPECFEM3D, has effectively resolved the expensive computational cost of 3D time-domain wave analyses of a coupled solid-fluid system, arising in global-scale seismology and geophysical inversion simulations [25–35]. SPECFEM3D has been rigorously benchmarked using reference analytical and numerical solutions [25, 30, 36, 37] and validated using real seismogram data [38, 39]. Thus, we are confident that SPECFEM3D is as trustable as commercial software, such as COMSOL and ANSYS.

This paper shows the applicability of SPECFEM3D in solving close-range wave propagation problems in an in-water pile driving environment with axially-asymmetric geometries of a pile and a surrounding solid domain. The reflection and refraction waves in such settings will affect the amplitudes of underwater piling noises. Because SEM can take into account complex geometries and arbitrary material heterogeneity of close-in harbor environments with uneven (sloped) sediment surfaces, this work would contribute to the body of knowledge in the area of computing underwater piling noises. We model sediment as a solid so that the resulted wave solutions are as realistic as possible. The need to model the solid sediment-fluid interaction was already suggested by Reinhall and Dahl [1], who had mentioned the importance of the accurate elastic description of the sediment, including shear deformation. The material properties of sediment (i.e., a geoacoustic model) should be guessed or be characterized by a non-destructive material-property characterization test. The latest advancement of full-waveform inversion theories [40–43] will enable such a non-destructive material characterization of sediment by using a field test with a mild sonar wave as an incident wave. This SEM-based modeling could be used for investigating novel engineering methods, such as an optimized design of an axially-asymmetric cross section of a pile and usage of air bubble curtains around a pile in axially-asymmetric settings (e.g., harbor environments in close proximity of harbor walls). These measures would be aimed to mitigate and reduce adverse impacts from piling noise.

2. Problem Definition

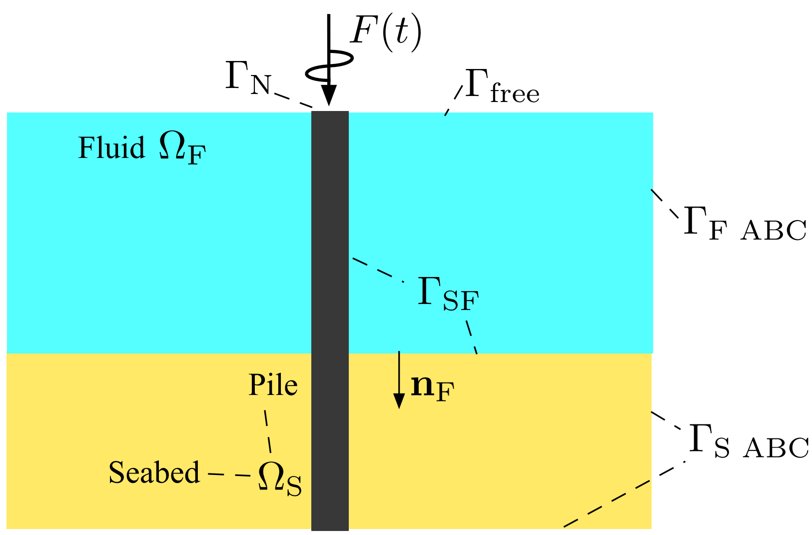

Fig. 1. The schematic diagram of an underwater pile driving. A fluid domain Ω_{F} and a solid domain Ω_{S} are truncated by absorbing boundaries $\Gamma_{\mathrm{F\ ABC}}$ and $\Gamma_{\mathrm{S\ ABC}}$, respectively. Because of the absorbing boundary at the bottom of a pile, only downward-propagating elastic waves in the pile are computed in the presented simulations. Fluid-solid coupling is considered on Γ_{SF}. A dynamic force $F(t)$ is applied at the center of Γ_{N}, and acoustic pressure vanishes on Γ_{free}.

We are interested in computing dynamic responses in a physical domain, comprised of water (fluid), seabed (solid), and a pile (solid), shown in Fig 1, by using the SEM. The fluid (Ω_{F}) is coupled with the solids (Ω_{S}) via solid-fluid interface Γ_{SF}. The absorbing boundary conditions truncate the domain. A dynamic force $f(t)$ is applied at the top surface (Γ_{N}) of the pile, and the top surface of the fluid is assumed to be a pressure release surface. In this study, we investigate the dynamic behavior of this physical system with the dynamic force

$f(t)$ acting vertically on the top of the pile.

The displacement field $\mathbf{u}_\mathrm{S}(\boldsymbol{x}, t)$ in elastic domains Ω_S (i.e., a pile and seabed) is governed by the equation:

$$\boldsymbol{\nabla} \cdot \mathbf{T} - \rho\, \partial_t^2\, \mathbf{u}_\mathrm{S} = 0 \quad , \tag{1}$$

where ρ denotes mass density, and $\mathbf{T}$ is the stress tensor. The stress tensor $\mathbf{T}$ is proportional to the strain, through the constitutive relationship:

$$\mathbf{T} = \mathcal{D} : \nabla \mathbf{u}_\mathrm{S} \quad , \tag{2}$$

where $\mathcal{D}$ denotes the elastic tensor that accounts for the elastic properties of each domains. The elastic tensor is in a general form, where a fully-anisotropic tensor with 21 independent parameters can be utilized [36]. We assume small deformation, thus, a linear constitutive relationship is valid. When this is not appropriate, a nonlinear constitutive relationship can be used. One case of interest would be the near-field soil around a pile if it is expected to undergoes plastic deformation. Although the nonlinear behavior could be integrated into the simulation, it is beyond the scope of the presented research. In addition, although the SPECFEM3D has a capacity of modeling the attenuation of elastic and acoustic waves, we do not consider the attenuation in this study because we are mainly concerned with the close-range piling noise. Within the ranges and frequency contents of the force signal presented in this paper, the attenuation should not be significant.

The boundary condition at the top surface Γ_N of a pile, where a point load $F(t)$ is applied, is given by:

$$\mathbf{T} \cdot \mathbf{n}_\mathrm{S} = \left[0\ 0\ {-F(t)}\right]^\mathsf{T} \delta(\boldsymbol{x} - \boldsymbol{x}_c) \quad , \tag{3}$$

where $\mathbf{n}_\mathrm{S}$ denotes the unit outward normal from the solid surface, δ is a Dirac delta, and $\boldsymbol{x}_c$ denotes the geometric center of the top surface of a pile. The body waves in solids are comprised of, primarily, P- and S-waves. The P-wave is a compressional wave, and its particle movement orientation is aligned with the propagating direction. The S-wave is known as a shear wave and is formed by shear deformation of a solid. Its particle movement orientation is perpendicular to the direction of wave propagation, and it is typically slower in speed than the P-wave.

In an acoustic domain, the particle displacement of fluid $\mathbf{u}_\mathrm{F}$ can be written as:

$$\mathbf{u}_\mathrm{F} = \rho^{-1} \boldsymbol{\nabla} \chi \quad , \tag{4}$$

where χ is defined as the scalar displacement potential. The acoustic wave motion in fluid Ω_F is formed by alternating compressions of fluid particles. The equation of motion in terms of the potential χ is:

$$\kappa^{-1} {\partial_t}^2 \chi = \boldsymbol{\nabla} \cdot (\rho^{-1} \boldsymbol{\nabla} \chi) \quad , \tag{5}$$

where ρ is the mass density; κ is the bulk modulus of the fluid. The pressure field can be obtained, after computing χ in the domain Ω_F, as:

$$P = -\kappa \boldsymbol{\nabla} \cdot \mathbf{u}_\mathrm{F} = -\partial_t^2 \chi \quad , \tag{6}$$

where P is the pressure field of the wave motion of fluid. The boundary condition of a fluid domain on its free surface (Γ_{Free}) is:

$$P = 0 \quad . \tag{7}$$

Noting that (7) is equivalent to $P = -\partial_t^2 \chi = 0$, χ vanishes on Γ_{Free}.

Between the interface (Γ_{SF}) of the solid and fluid domains, the normal traction $\mathbf{T} \cdot \mathbf{n}_{\text{S}}$ and the normal component of displacement (i.e., $\mathbf{u}_{\text{S}} \cdot \mathbf{n}_{\text{S}}$) need to be continuous as:

$$\mathbf{T} \cdot \mathbf{n}_{\text{S}} = P\, \mathbf{n}_{\text{F}} = -\partial_t^2 \chi\, \mathbf{n}_{\text{F}} \quad , \tag{8}$$

$$\mathbf{u}_{\text{S}} \cdot \mathbf{n}_{\text{S}} = -\rho^{-1} \boldsymbol{\nabla} \chi \cdot \mathbf{n}_{\text{F}} \quad , \tag{9}$$

where $\mathbf{n}_{\text{F}}$ and $\mathbf{n}_{\text{S}}$ denote the unit outward normals from the fluid and solid surfaces, respectively, at the interface Γ_{SF}, and $\mathbf{T} \cdot \mathbf{n}_{\text{S}}$ denotes the traction field vector of the wave response of a solid particle. Equation (8) shows that the traction field of a solid has a non-zero value only in a normal component, which is equal to $P\, \mathbf{n}_{\text{F}}$. The tangential component (i.e., friction) of the traction field at the fluid-solid interface is zero because there is no shear friction between the solid and the fluid. Also, as represented in (9), the normal component of the displacement field of the solid at the fluid-solid interface is equal to that of the fluid at the interface, while the tangential component of displacement field of the solid differs from that of the fluid at the interface. In addition, we use Clayton-Engquist-Stacey absorbing boundary conditions [44,45] to absorb outgoing waves on boundaries (Γ_{ABC}) of the domain, representing a semi-infinite extent:

$$\boldsymbol{\nabla} \chi \cdot \mathbf{n}_{\text{F}} = -V_{\text{F}}^{-1} \partial_t \chi \quad \text{on } \Gamma_{\text{F ABC}} \quad , \tag{10}$$

$$\mathbf{T} \cdot \mathbf{n}_{\text{S}} = \rho \left(V_p\, \partial_t \mathbf{u}_{\text{S}}^{\text{n}} + V_s\, \partial_t \mathbf{u}_{\text{S}}^{\text{t}} \right) \quad \text{on } \Gamma_{\text{S ABC}} \quad , \tag{11}$$

where V_{F} denotes the wave speed of the acoustic wave. Similarly, V_p and V_s are the P- and S-wave speeds, respectively, in the solid domain; and $\partial_t \mathbf{u}_{\text{S}}^{\text{n}}$ and $\partial_t \mathbf{u}_{\text{S}}^{\text{t}}$ are, respectively, normal and tangential velocity components of a solid particle's movement. Lastly, to initiate the simulation at rest, the initial conditions are:

$$\mathbf{u}_{\text{S}}(\boldsymbol{x}, 0) = \mathbf{0} \quad , \quad \partial_t \mathbf{u}_{\text{S}}(\boldsymbol{x}, 0) = \mathbf{0} \quad \text{in } \Omega_{\text{F}} \quad , \tag{12}$$

$$\chi(\boldsymbol{x}, 0) = 0 \quad , \quad \partial_t \chi(\boldsymbol{x}, 0) = 0 \quad \text{in } \Omega_{\text{S}} \quad . \tag{13}$$

We solve the governing wave equations shown in this section by using the SEM. We omit the detailed procedure of SEM in this paper because the theoretical and computational aspects of the SEM procedure are well known and can be found in a number of papers [25, 26, 28–34, 46]. In particular, the SEM procedure for the coupled fluid-solid media can be seen in recent papers [24, 47, 48].

We approximate the curved geometry of the elements by using the second-order shape functions and the solution function (χ and $\mathbf{u}_{\text{S}}$) by using the fourth-order shape functions. To obtain numerical solutions of wave responses accurately, we carefully determine the spatial and temporal discretizations of models in the following manners. First, the size of an element should be determined in a manner such that at least 8 nodes exist within the smallest wavelength $V_{\min}/f_{\max}$ [49]. Here, $V_{\min}$ is the smallest wave speed in the domain and $f_{\max}$ denotes the maximum discernible frequency of an excitation. Second, to obtain the stable time-domain solution of the simulation, the time step Δt should satisfy the following Courant stability condition [50]:

$$\Delta t \leq C_{\max}\left(\frac{h}{V_{\max}}\right) \quad , \tag{14}$$

where h denotes the distance between the adjacent grid points and $V_{\max}$ denotes the maximum wave speed. $C_{\max}$ is the maximum Courant number, which should be 0.5 for regular meshes and 0.3 to 0.4 for very irregular meshes with distorted elements and strong heterogeneity, respectively [46].

3. Numerical results

This section presents the numerical results of close-range offshore piling noise simulated by using the SEM wave solver in various settings. In Case 1, we describe underwater piling noise for an axially-symmetric pile in a horizontally-unbounded domain. Case 2 shows the dependency of the close-range piling noise on cross-sectional geometries of piles. Case 3 shows the reflection of underwater piling noise in an axially-asymmetric surrounding solid domain. Case 4 presents the applicability of using the SEM for computing piling noise in a harbor-like domain. To simulate the Cases 1 to 4, we used a high-performance computing (HPC) Dell workstation, with twelve Intel Xeon CPU processors (2.6 GHz) and 128 GB RAM memory. An advanced mesh generator Trelis was used for creating meshes. For all the cases, each simulation took about 4 hours when we used eight CPU cores and 128 GB RAM memory.

3.1. *Case1: Axially-symmetric pile in a horizontally-unbounded domain*

This example considers an in-water pile driving environment that is a cube of 10 meters on each side (see Figure 2). This volume is divided horizontally in the middle to separate the fluid and seabed domains. A 10-m long solid cylindrical pile of 1-m diameter is located at the center of the cube. The density of the fluid domain, assumed to be seawater, is 1030 kg/m^3 with a P-wave speed of 1500 m/s. The seabed is composed of homogeneous saturated shales and clays. The Stanford Rock Physics Laboratory [51] gives the density for this material as 2200 kg/m^3 with a P-wave speed of 1800 m/s and an S-wave speed of 625 m/s. The cylindrical pile is made of steel, which has a mass density of 8050 kg/m^3 with P-wave and S-wave speeds of 5790 m/s and 3100 m/s, respectively. A downward point load is applied at the top center of the pile. A Ricker pulse, shown in Figure 3(A), is employed to represent the broadband impact pulse acting at the center on the top surface of the pile [52]. The central frequency of the Ricker impact source signal is 2.5 kHz and its maximum amplitude is 10 kN. Although an actual force signal could differ from this synthetic Ricker pulse signal, we used the Ricker signal because of its broadband frequency contents (see Figure 3(B)). A total calculation duration is 4 ms, and a time step is 2×10^{-4} ms. Absorbing boundary

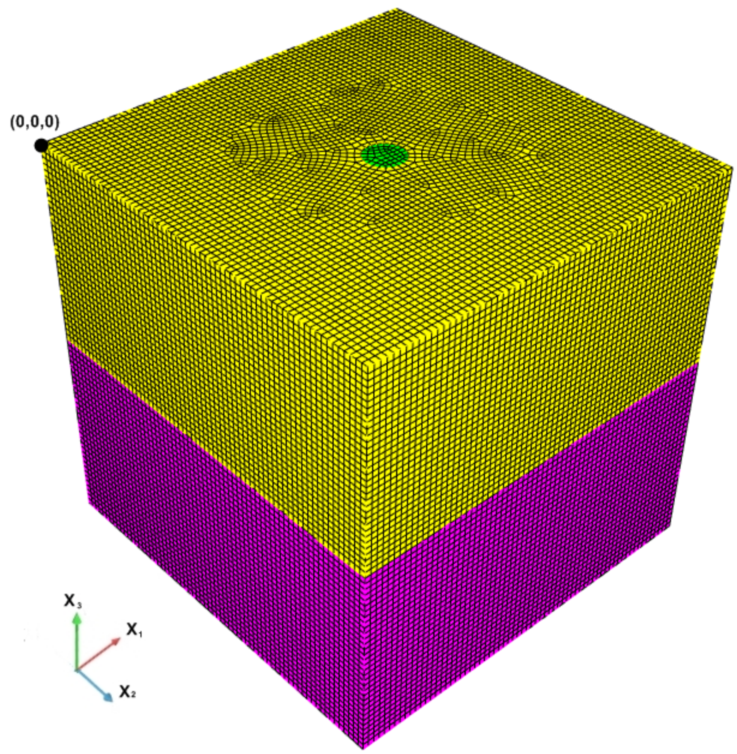

Fig. 2. Case 1: A computational domain. The fluid domain is shown in yellow, the seabed is shown in magenta, and the pile is shown in green.

conditions were imposed at the bottom and side surfaces of the cube domain to model the semi-infinite extents. We applied a pressure release condition at the sea surface. The average element size is nearly 0.15 m in the entire domain (see Figure 4). The smallest wavelength is 0.25 m, which is obtained by dividing 625 m/s (i.e., the smallest S-wave speed in solids) by the Ricker pulse's central frequency of 2.5 kHz. The smallest wavelength is modeled by using 8 nodes in this simulation. For these element and time step sizes, the maximum length of a cube domain is limited to about 10 m for a workstation with the 128 GB RAM memory.

Sensor	x_1 (m)	x_2 (m)	x_3 (m)
1	3.0	5.0	-2.5
2	1.5	5.0	-2.5

Table 1. Locations of sensors in Cases 1 and 2.

Figure 5 shows the results obtained in SPECFEM3D simulation at every 0.5 ms. It illustrates how the hydroacoustic waves propagate from the impact location at the topmost center of the pile to the domain's boundaries and how acoustic waves propagate symmet-

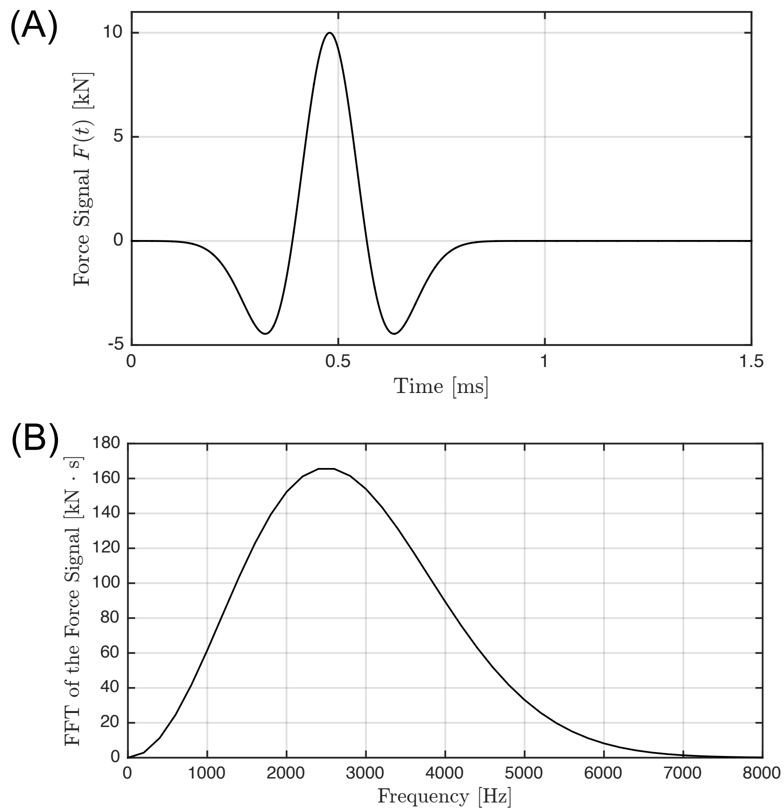

Fig. 3. (A) A Ricker wavelet used as an impact signal force signal and (B) its frequency content.

rically in x_1 and x_2 directions. The waves propagate in a cone-like shape, also known as a Mach Cone, which is a conical pressure wave front produced by a moving sound source whose moving speed is greater than that of sound. To wit, while the elastic wave propagates downward in a solid pile at a faster speed than that of an acoustic wave, the elastic wave-induced vibration in the pile acts as a moving train of acoustic wave sources and creates a Mach Cone in the surrounding fluid. The angle between the Mach Cone and the pile surface can be analytically calculated as the following (see Figure 6):

$$\theta = \sin^{-1}\left(\frac{V_{\text{acoustic wave}}}{V_{\text{elastic wave (P or S) in a pile}}}\right), \tag{15}$$

where $V_{\text{elastic wave (P or S) in pile}}$ and $V_{\text{acoustic wave}}$ denote the speeds of waves in the pile and its surrounding acoustic fluid, respectively. If the pile is surrounded by sediment, the numerator in the above (15) should be replaced by the speed of P- or S-wave in sediment in order to compute the angles of Mach Cones in sediment. Figure 5 shows six different Mach Cones with their angles with respect to the pile surface. Specifically, Mach Cones 1 to 6 denote those induced by the differences of the following waves' speeds, respectively: (i) the acoustic

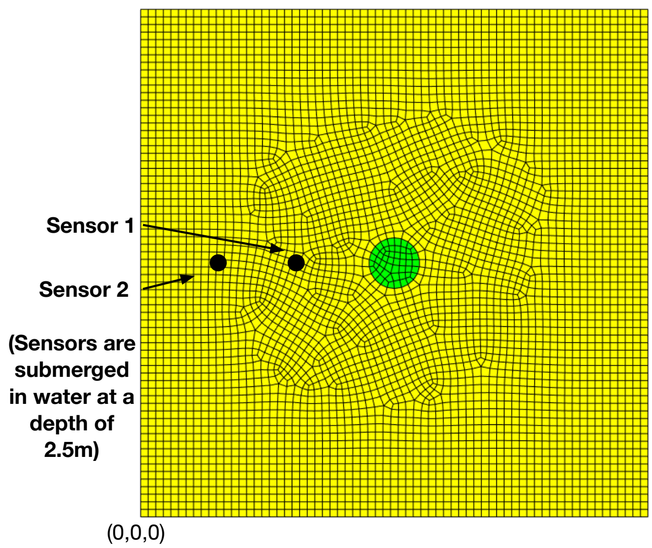

Fig. 4. Case 1: Mesh (top view).

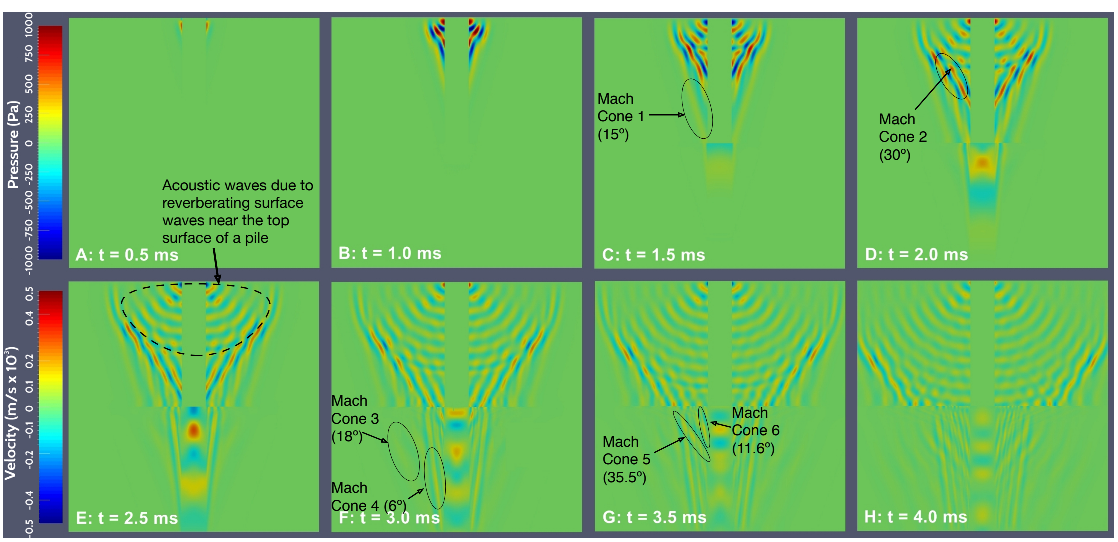

Fig. 5. Case 1: Acoustic pressure field P (Pa) of acoustic waves in fluid in the upper half of each figure and x_3-directional velocity field $\partial_t u_{S_3}$ (m/s) of elastodynamic waves in solid in the lower half of each figure. Plots shown in x_1x_3-plane. The upper color bar shows the scale of pressure, and the lower one shows that of velocity. Figs. 9, 10, and 16 are plotted similarly.

wave and the P-wave in the pile; (ii) the acoustic wave and the S-wave in the pile; (iii) the P-wave in the sediment and the P-wave in the pile; (iv) the S-wave in the sediment and the P-wave in the pile; (v) the P-wave in the sediment and the S-wave in the pile; and (vi) the

S-wave in the sediment and the S-wave in the pile. The angles between the Mach Cones 1 to 6 and the pile surface are measured to be 15°, 30°, 18°, 6°, 35.5°, and 11.6°, respectively, as shown in Figure 5. These numerically-computed values are in good agreement with the values theoretically evaluated by (15).

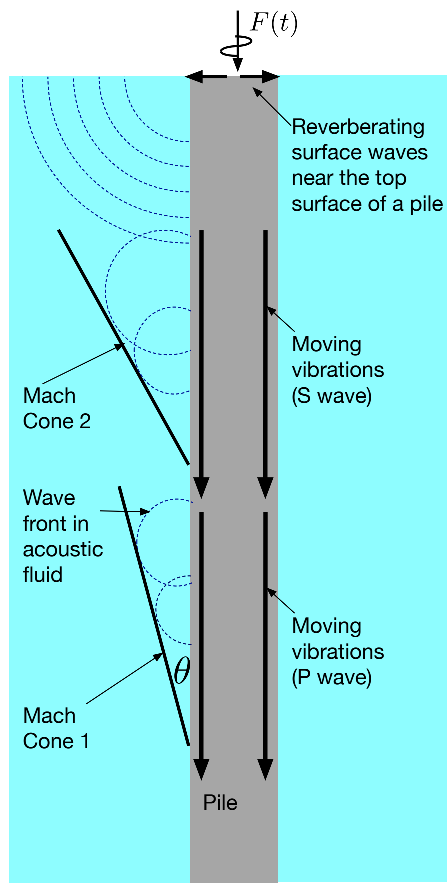

Fig. 6. Waves occurring in a pile and its surrounding fluid. The elastic wave-induced vibration in a pile acts as a fast-moving acoustic wave source and creates a Mach Cone in the surrounding fluid.

The annotation in Figure 5 at $t = 2.5$ ms shows the acoustic waves in fluid induced by reverberating surface waves near the top surface of a pile. The reverberating surface waves occur because we applied a point loading at the center of the top surface of the pile (see the upper part of Figure 6). Figure 5 also shows that the absorbing boundary conditions were effective in the simulations as no discernible reverberations can be seen on the bottom and side boundaries. In addition, Figure 5 shows that acoustic pressures are greater near the surface of the pile than at the large distance.

In this paper, the maximum amplitude of an impact force on the pile is set to be 10 kN, and it is applied at the single node on the centroid of the top surface of a pile. We note that the maximum amplitude of the impact force in this work is much smaller than that in other previous works. For instance, in the benchmark example in the COMPILE workshop [23], the maximum amplitude of an impact force signal was set to be 20 MN (2,000 times higher than ours). This force was applied as its equivalent distributed load on the top surface of a hollow circular pile. Because of the small order of magnitude of our force signal, the order of magnitude of fluid pressure computed at sensor 2 (3.5 m away from a pile in a radial direction at a depth of 2.5 m) is about 300 Pa. On the other hand, the COMPILE workshop's benchmark counterpart computed at a sensor (11 m away from a pile in a radial direction at a depth of 5 m) is about 60000 Pa, which is 200 times larger than ours: its equivalent one at 3.5 m away from a pile in a radial direction turns out to be about 1975 times larger than ours by multiplying 60000 Pa by $\frac{11^2}{3.5^2}$. Here, the ratio of 1:1975 between the order of magnitude of the wave response in our paper to its counterpart in the COMPILE workshop closely matches that of 1:2000 between the order of magnitude of an impact force signal in our paper to its counterpart in the COMPILE workshop [23]. In summary, although the amplitude of wave responses in this paper is much smaller than that of the reference numerical solution, they are acceptable given the difference in detailed problem settings (e.g., the magnitude of an impact force signal and the depth of water).

The computed acoustic pressures are employed to determine sound pressure levels (SPL) defined as:

$$\mathrm{SPL} = 10 \log_{10} \left(\frac{P^2}{{P_{\mathrm{ref}}}^2} \right) \quad , \tag{16}$$

where P is the pressure from our SEM simulation, while P_{ref} is the reference pressure in water (P_{ref} is 1 μPa in our numerical simulations). The sound exposure level (SEL) can also be calculated using the SEM results by:

$$\mathrm{SEL} = 10 \log_{10} \frac{1}{T_0} \int_{t_1}^{t_2} \left(\frac{P^2}{{P_{\mathrm{ref}}}^2} \right) dt \quad , \tag{17}$$

with $T_0 = 1$ second is the reference time internal length. Although it is possible to show the spatial distributions of SEL, we show only the snapshots of SPL distributions in this paper. Figure 7 shows the distribution of SPL over the fluid domain at every 0.5 ms in this Case 1. From time $t = 2.5$ ms to $t = 4.0$ ms, lateral interface waves were generated at the interface between the fluid and the seabed (see the snapshots at t = 2.0, 2.5, 3.0, and 3.5 ms in Figure 7). There are two reasons why these waves are generated. First, once the Mach Cone of acoustic waves hits the sediment-fluid interface, it excites the underlying sediment. The resulted waves in the sediment propagate faster along the interface than the acoustic wave and, in turn, excite the fluid above the interface. Second, the Mach Cone of the elastic wave in the seabed (see the snapshots at t = 2.5, 3.0, and 3.5 ms in Figure 5) arrives at the seabed-water interface and generates acoustic waves along the interface.

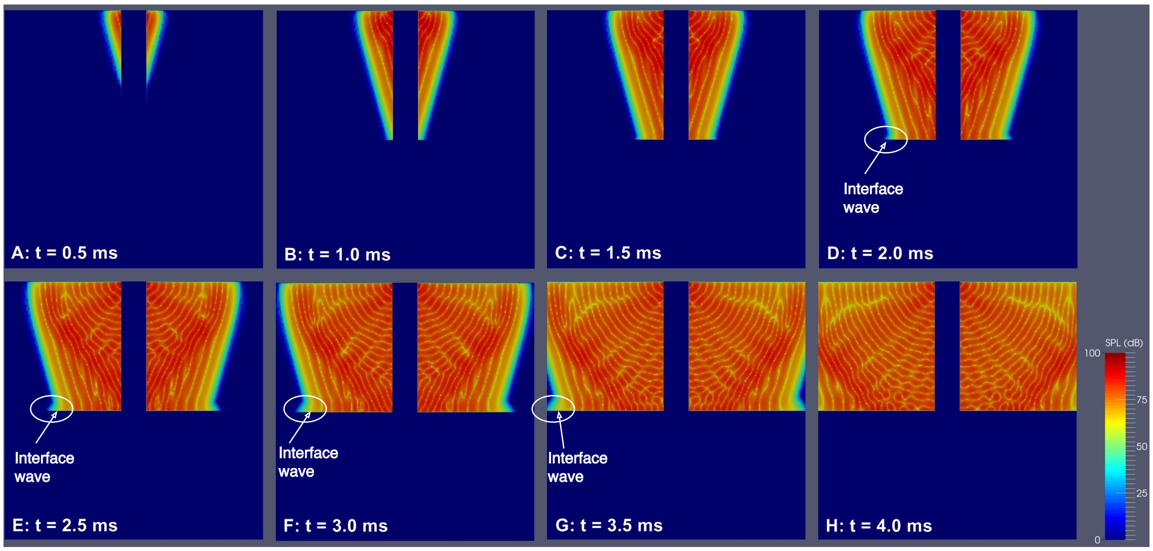

Fig. 7. Case 1: Snapshots of SPL (dB re 1 μPa) in acoustic domain.

3.2. *Case 2: Piles with non-circular cross sections in a horizontally-unbounded domain.*

While most papers, related to underwater piling noise modeling, only consider cylindrical piles, this section considers piles with non-circular cross sections. For these examples, we consider piles with square and triangular cross sections. Figure 8 provides the top view of each meshed geometry. The cross sections of both square and triangle shapes have the same area size (0.25π m^2) as the circular pile considered in Case 1. All other properties of the water, seabed, and pile are identical to Case 1 for the reasonable comparison between Cases 1 and 2, highlighting the effect of a cross-sectional geometry of a pile on the piling noise.

Figures 9 and 10 show the side-view snapshots of the pressure waves in the fluid domain for the piles with square and triangular cross sections, respectively. Wave propagation behaviors for the two models significantly differ from each other. Figures 11 and 12 illustrate the distribution (top view) of SPL for the three different geometries of pile cross sections at a fluid depth of 2.5 m. These figures show that the shapes of wave fronts of hydroacoustic wave vary for each geometry of a pile cross section. For instance, the wave front for an axially-symmetric pile is radially symmetric, and its high SPL values are distributed evenly around the surface of the pile. In contrast, for axially-asymmetric piles, wave fronts are highly irregular, and their associated SPL values are not distributed evenly.

Figure 13 also provides the comparison of hydroacoustic pressures measured at Sensors 1 and 2 for all the pile shapes in Cases 1 and 2 (see Table 1 for the coordinates of each sensor). Figure 13(A) shows that the maximum absolute pressure occurred in a cylindrical pile simulation was 425 Pa at Sensor 1. The square cross-section pile generated a maximum absolute pressure of 519 Pa at Sensor 1. Amongst all the models, the triangle cross section

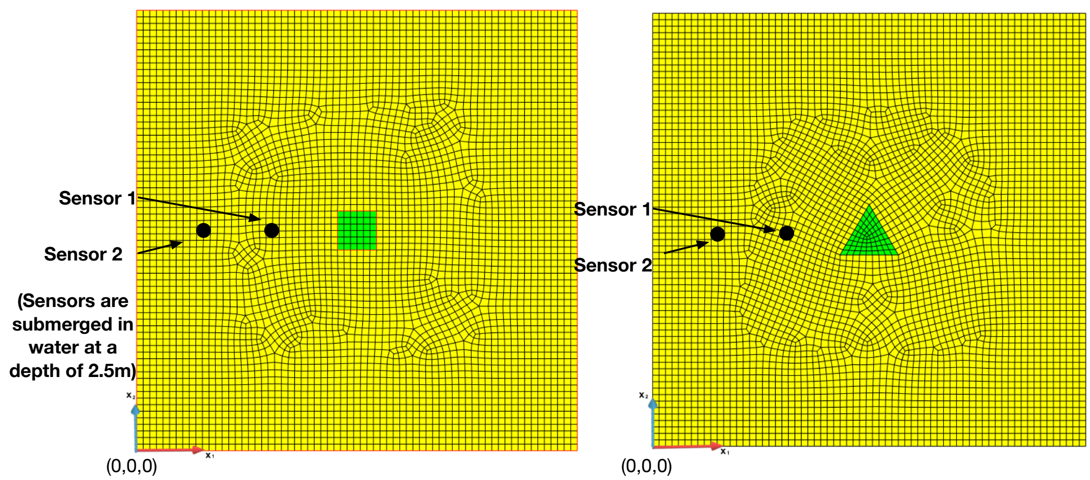

Fig. 8. Case 2: Mesh configuration for piles of square- and triangle-shaped cross sections (top view). The fluid domain is shown in yellow, and the piles are shown in green.

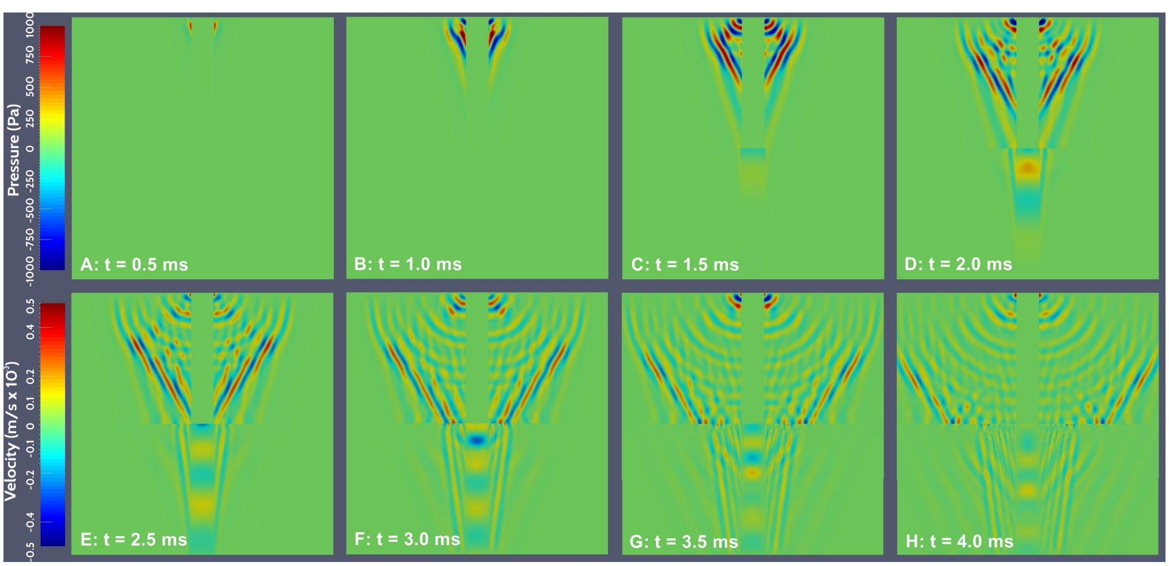

Fig. 9. Case 2, square-shaped pile: Snapshots showing P (Pa) of acoustic waves in fluid in the upper half of each subfigure and $\partial_t u_{S_3}$ (m/s) of elastodynamic waves in solid in the lower half of each subfigure. Plots shown in x_1x_3-plane (refer to the Cartesian coordinate system in Figure 2).

pile produced the highest absolute pressure equal to 808 Pa at Sensor 1, twice that of the cylindrical pile model. Figure 13(B) shows that the maximum acoustic pressures for the circular, square and triangle cross-section pile simulations were 338 Pa, 549 Pa and 467 Pa, respectively, at Sensor 2. These results show that the cross-sectional shape of a

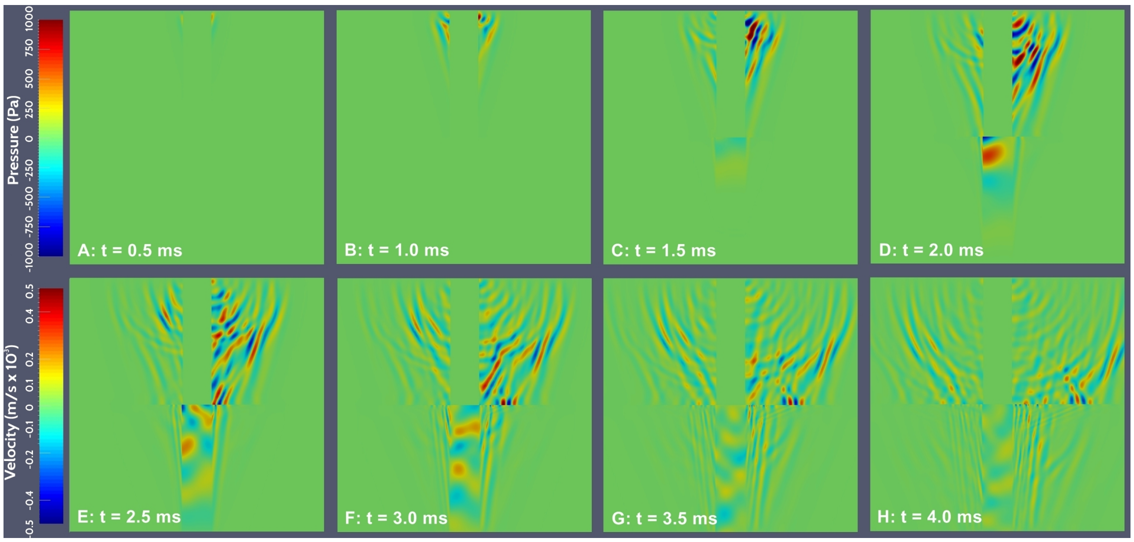

Fig. 10. Case 2, triangular-shaped pile: Snapshots showing P (Pa) of acoustic waves in fluid in the upper half of each subfigure and $\partial_t u_{\mathrm{S}_3}$ (m/s) of elastodynamic waves in solid in the lower half of each subfigure. Plots shown in $x_1 x_3$-plane.

pile influences the intensity of underwater piling noise in the close range. Among the three pile cross-sectional shape models, the triangular cross-section pile resulted in the highest hydroacoustic pressure at Sensor 1. However, the square-shaped cross-section pile generated the highest magnitude of hydroacoustic pressure at Sensor 2. This behavior was caused by wave interferences that the axially-asymmetric piles led to.

The simulations in this Case 2 suggest that changing the cross-sectional shape of a pile could affect (possibly reduce or increase) the magnitude of underwater piling noise in the close range. For instance, we could examine a pile with a band gap in the outward radial direction, using optimized cross-sectional shapes, that can significantly attenuate the propagation of waves in the outward radial direction of a pile. The band gap could be designed around the predominant frequency band of an actual piling force signal. The band gap could be made by not only the geometrical designs but also the material composition of a pile. The material properties of a pile could affect the amplitudes of underwater piling noises. For instance, suppose that a pile consists of two different materials: the outer layer of a pile is made of steel and its inner core is made of concrete, of which P- and S-wave speeds (e.g., 3174 and 1851 m/s) are smaller than those of steel (5790 and 3100 m/s) [53]. Then, a larger impact wave energy could be delivered into the inner core of this pile than a homogeneous pile. It is well known that wave energy is, in general, concentrated in an area whose wave speeds are smaller than its neighboring areas (i.e., the waveguide effect) [54]. Thus, the intensity of radiating acoustic waves from this composite pile into the water could be smaller than that of a homogeneous, non-hollow pile. Of course, SEM-based structural optimization studies, determining the best combination of topography and material properties of a pile, could result in a pile that can more effectively reduce noise than our suggested simple

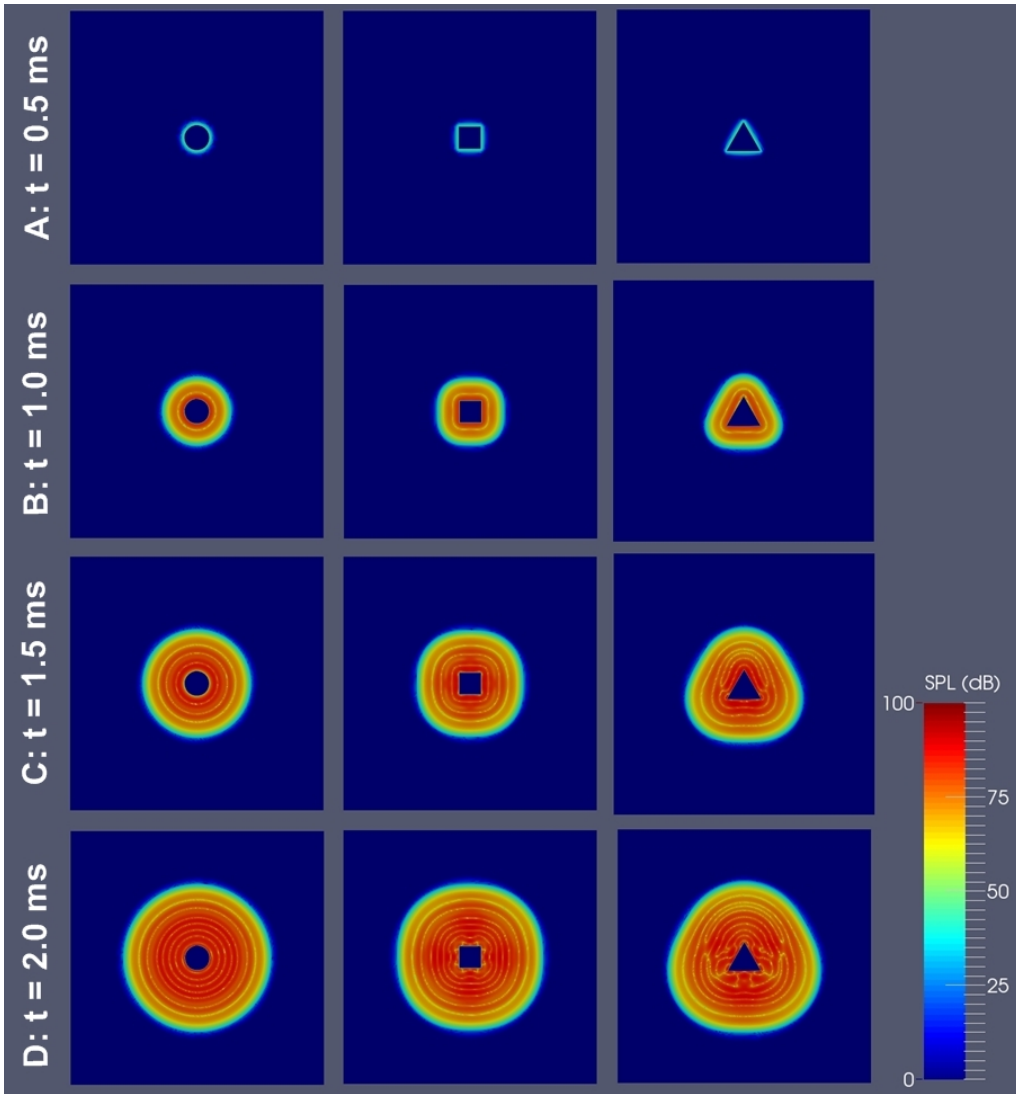

Fig. 11. Snapshots of SPL (dB re 1 μPa) at depth x_3 = -2.5 m at every 0.5 ms in the acoustic domain.

concrete-steel pile. In addition, the structural performance of piles with non-circular cross-sectional geometries, induced by quasi-static or low-frequency dynamic loadings, and their associated strengths should be studied and compared with those of circular piles in the future.

3.3. *Case 3: Axially-asymmetric surrounding solid domain*

In-water pile driving in axially-asymmetrical environments, such as harbors, streams, or riverbanks, could generate complex wave responses mainly due to wave reflections at bounding regions. Figure 14 shows an axially-asymmetric domain with side walls, and Figure 15

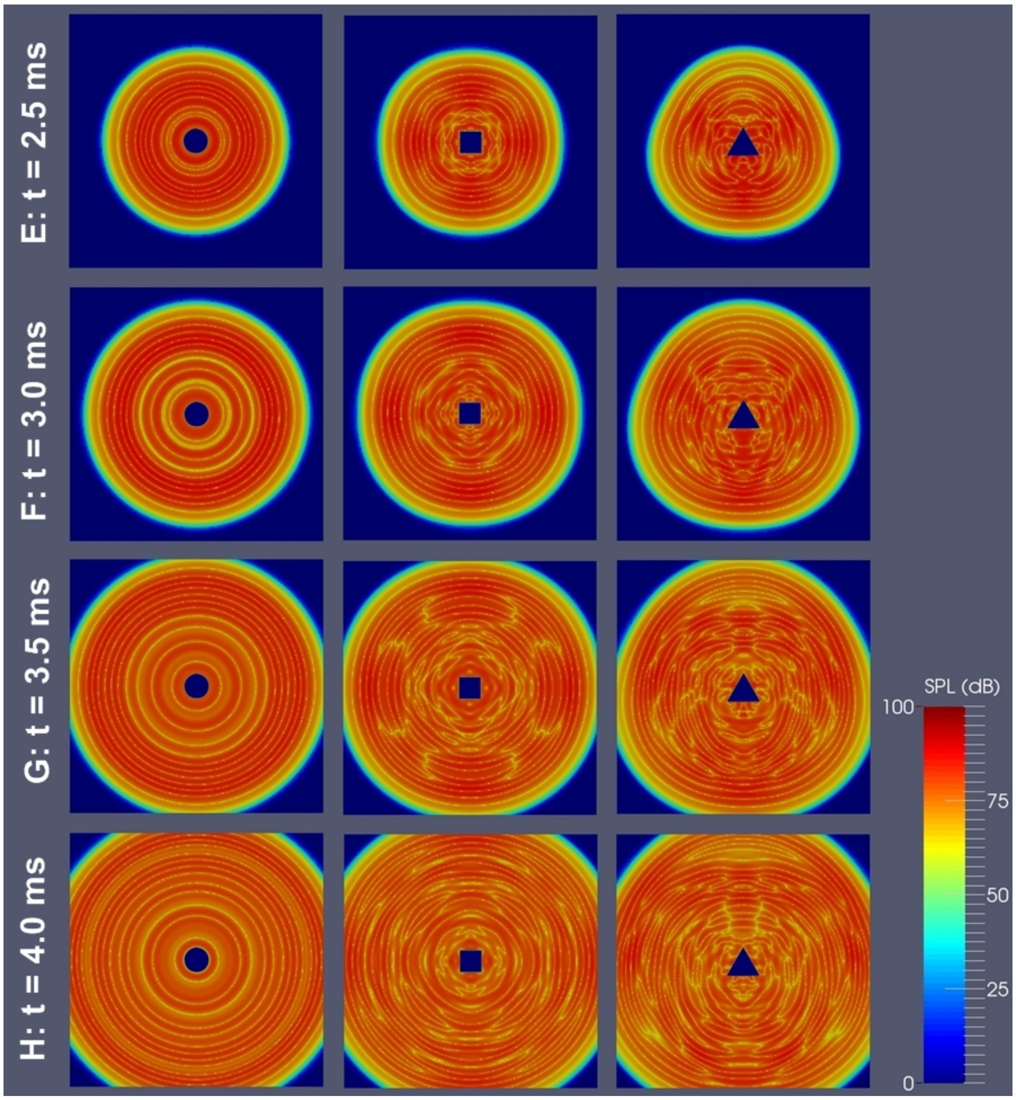

Fig. 12. Snapshots of SPL (dB re 1 μPa) at depth x_3 = -2.5 m at every 0.5 ms in the acoustic domain.

shows its top view. A cylindrical pile is located at the center of a 10 m cubic domain, and 1.25 m thick side walls are included on two sides. The material properties of the walls are assumed to be those of the underlying seabed in order to investigate only the effect of wave reflection from side walls. All other properties and mesh parameters are the same as those in Cases 1 and 2. In this paper, both the sediment and the surrounding walls are modeled as non-permeable (having no pore fluid) solids, and this work does not use a solid that is a perfectly-impenetrable barrier to sound (i.e., a sound hard material with the boundary condition $\frac{\partial P}{\partial \mathbf{n}_S} = 0$). The sound wave in fluid interacts with its neighboring solid so that it creates another elastic wave in the solid.

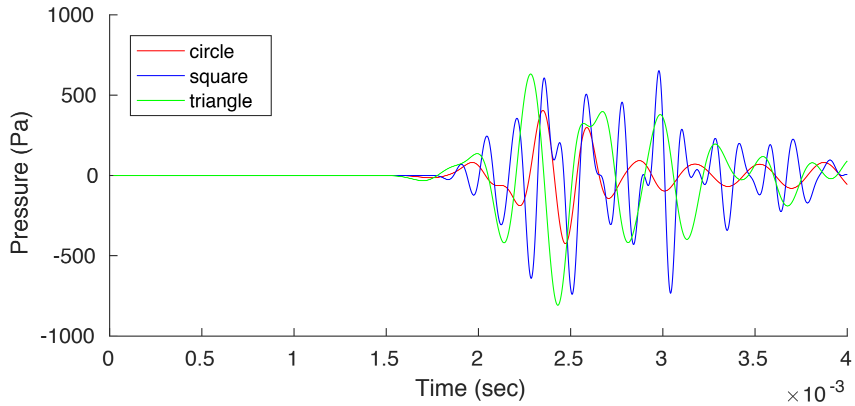

(A) Pressure at Sensor 1

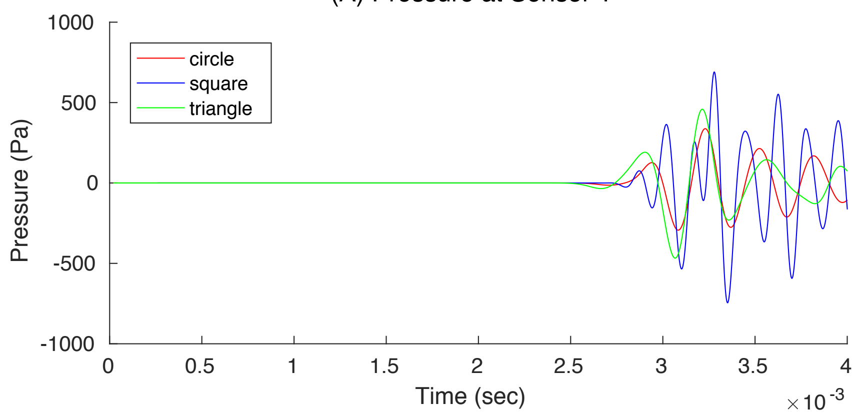

(B) Pressure at Sensor 2

Fig. 13. Acoustic pressure over time measured at Sensors 1 and 2.

Figure 16 shows the resulting acoustic pressure at time intervals of t = 0.5 ms while Figure 17 shows its equivalent SPL values at a cross section of depth, x_3 = -2.5 m. The behavior of pressure waves, from t = 0.5 to 2.0 ms, are similar to those in the axially-symmetric domain in Case 1. At t = 2.5 ms, the wave propagating in the fluid reaches the surrounding wall. At next time steps, t = 3.0 to 4.0 ms, the hydroacoustic pressure waves are reflected off the walls to the fluid domain, and result in a complex sound field because the waves from the pile interfere with those reflected from the walls.

We used a sensor to record pressures over time, and its location coordinates are the same as those of the Sensor 2 in Table 1. The sensor detected the increase (17% in P_{max} (Pa)) in the maximum pressure compared to that of the Sensor 2 in Case 1. Such an increase is caused by the reverberating pressure waves from the side walls.

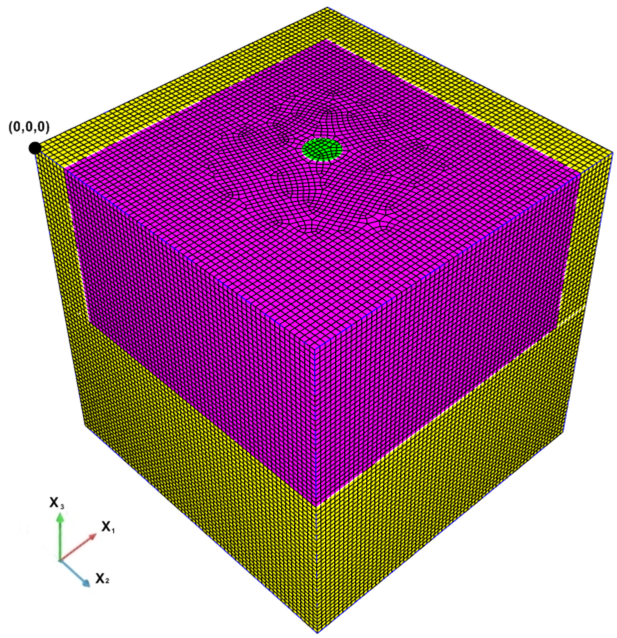

Fig. 14. Case 3: A surrounding solid domain of an axially-asymmetric geometry. The solid domain is shown in yellow, the fluid domain is shown in magenta, and the pile is shown in green.

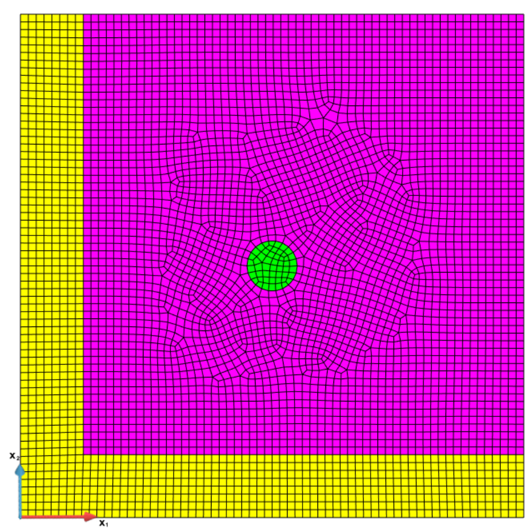

Fig. 15. Case 3: Domain with a solid-like wall (top view). The solid domain is shown in yellow, the fluid domain is shown in magenta, and the pile is shown in green.

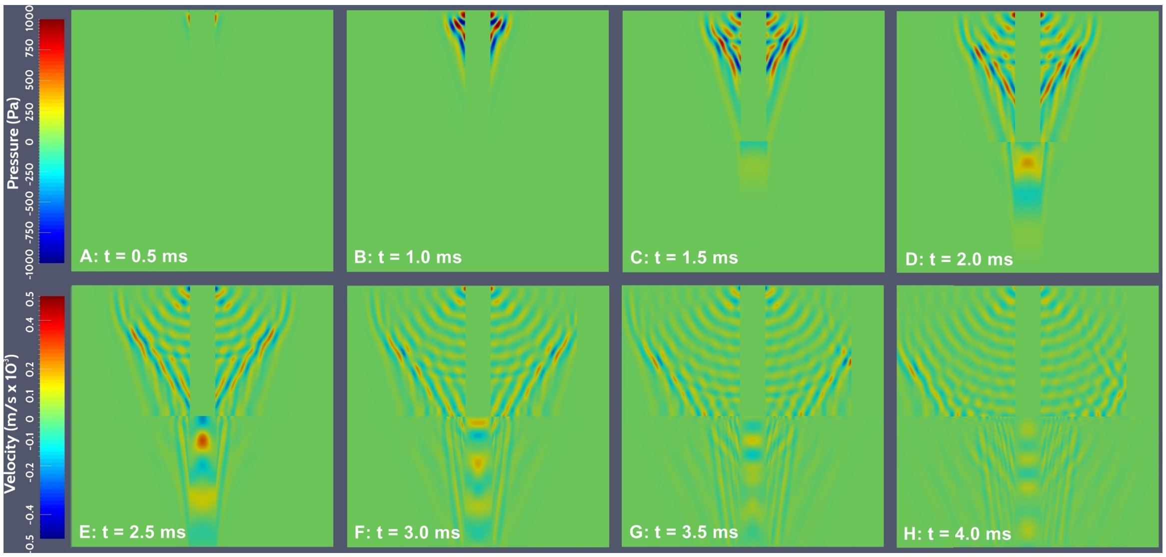

Fig. 16. Case 3: Snapshots showing P (Pa) of acoustic waves in fluid, in the upper half of each figure, and $\partial t u_{S_3}$ (m/s) of elastodynamic waves in solid, in the lower half of each figure. Plots shown in x_1x_3-plane.

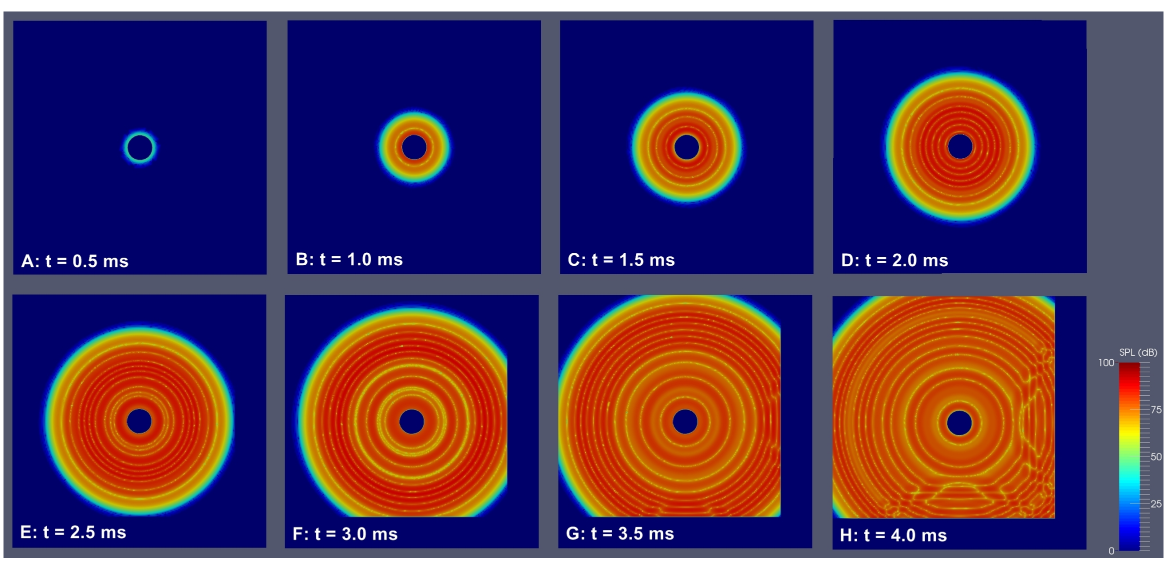

Fig. 17. Case 3: Cross section view of SPL (dB re 1 μPa) results at every 0.5 ms with an asymmtric solid domain and at depth, x_3 = -2.5 m.

3.4. *Case 4: Harbor-like domain*

The geometry for Case 4 was designed based on the study by Zampolli et al. [55], who validated the use of FEM in computing underwater piling noise by using experimental data.

They used Comsol and compared their FEM solution to field data collected on December 2-3 2010 at the IHC Hydrohammer Kinderdijk site in the Netherlands. Their study used a linear structural-acoustic model to approximate the behavior of underwater piling noise. They ignored the influence of harbor walls on the piling noise and used an axially-symmetric model to reduce the computational cost. They acknowledged that omitting the effects of harbor walls, bathymetry variations, and sub-bottom layering contributed to the difference between the measured data and their numerically-computed underwater noise. To investigate the influence of complex-shaped harbor walls on the hydroacoustic wave responses, we study a site condition that is similar to that studied by Zampolli et al. We do not compare this simulation to the actual field experiment data because some properties in this simulation are not similar to those used in the field experiment of Zampolli et al.'s study, and not all information (such as harbor wall properties) was available in their paper. Moreover, using the actual site dimension of a very large domain in their paper with elements of very small mesh sizes requires a higher computational cost than that available in a workstation with 128 GB RAM memory. Hence, we scaled down the site dimensions by half. We also simplified the site geometry by considering straight walls over curved ones given in the schematic representation of the trial site.

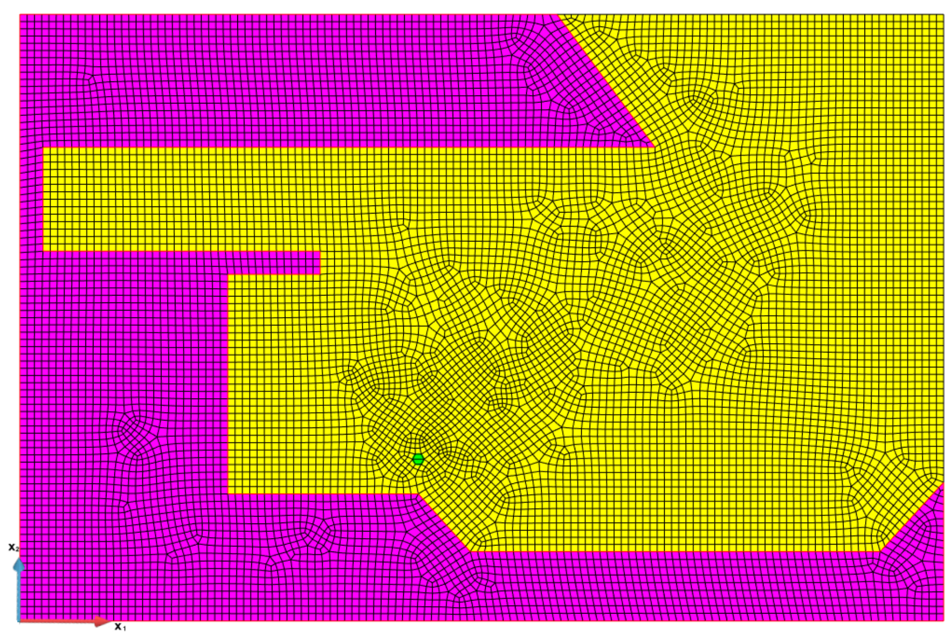

Fig. 18. Case 4: Top view of the harbor-like domain. The fluid domain is shown in yellow, the seabed is shown in magenta, and the pile is shown in green.

This work considered a domain that has a total length and width of 80.0 m and 52.5 m, respectively (see Figure 18). The total depth from the top surface to the bottom is 6.0 m, and the fluid region has a depth of 5.0 m from the top surface (see Figure 19). The pile still has a diameter of 0.5 m and a height equal to the domain's total depth. The side and bottom surfaces are truncated by using the absorbing boundaries.

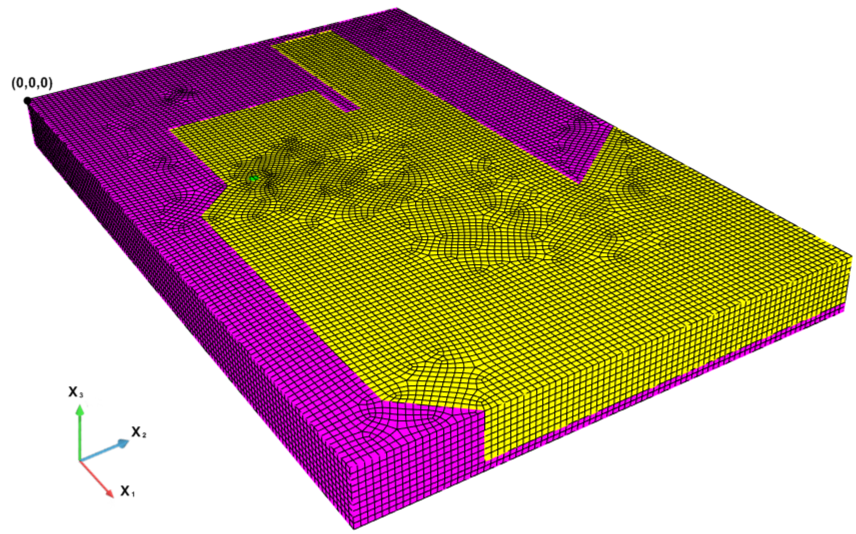

Fig. 19. Case 4: Isometric view of the harbor-like domain. The fluid domain is shown in yellow, the seabed is shown in magenta, and the pile is shown in green.

To reduce the computational cost, we used an average mesh size of 0.75 m, which is larger than the previous cases, and a Ricker pulse piling force signal of its central frequency 0.5 kHz. The 10 kN downward Ricker pulse force was applied at the top of the pile, which is located at $x_1 = 34.5$ m and $x_2 = 14.0$ m.

Figures 20(A) and (B) show the SPL results of this simulation at selected time interval from $t = 0.003$ s to $t = 0.015$ s at a section cut along the x_2-x_3 plane at $x_1 = 34.5$ m and a section cut along the x_1-x_3 plane at $x_2 = 14.0$ m, respectively. Similar to the results in previous cases, the underwater sound pressure starts as a conical shape, and then, expands over time, eventually reverberating back into the fluid region after reaching the harbor walls. Lastly, Figure 21 presents the SPL-converted pressure at the x_1-x_2 plane at $x_3 =$ -1.5 m. Harbor walls surrounding the pile greatly influence the acoustic waves. Waves reverberate after reaching the surface of the solid regions, causing complex wave responses and their constructive and destructive interferences. Using the conventional axially-symmetric FEM simulation cannot capture this phenomenon so that it causes disagreement between simulation results and experimental measurement data in harbor-like environments. Therefore, SEM should be employed for computing close-range piling noise in axially-asymmetric harbor-like settings.

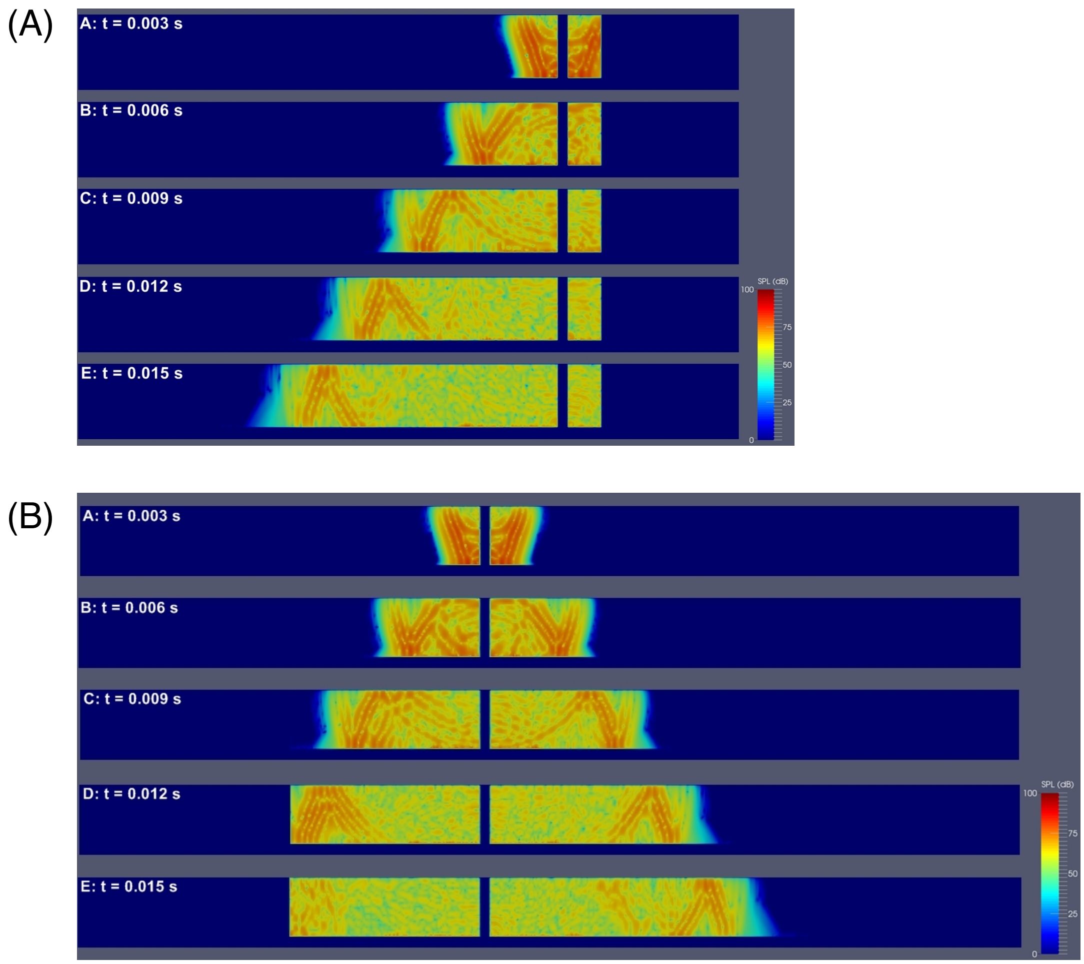

Fig. 20. Case 4: Cross section view of SPL at (A) x_1 of 34.5 m and (B) x_2 of 14.0 m ($0.003 \leq t \leq 0.015$ s).

4. Summary

This research presents the applicability of using SEM in computing the time-domain behavior of close-range underwater noise due to in-water pile driving in full 3D settings. This research shows that the solver's versatility can take into account the fluid-solid coupling, absorbing boundary conditions, and the pressure-free top surface of the fluid. We have presented various models, namely, piles of axially-asymmetric cross-sectional shapes and axially-asymmetric surrounding domains, and showed corresponding variations in underwater piling noise.

When an axially-symmetric circular pile is considered in a horizontally-unbounded setting (Case 1), the sound pressure wave in fluid initially propagates as a conical shape. This acoustic field is produced when impact-based stress waves travel in a pile of fast wave speeds that is surrounded by water of a slower speed of sound [1]. We showed that there

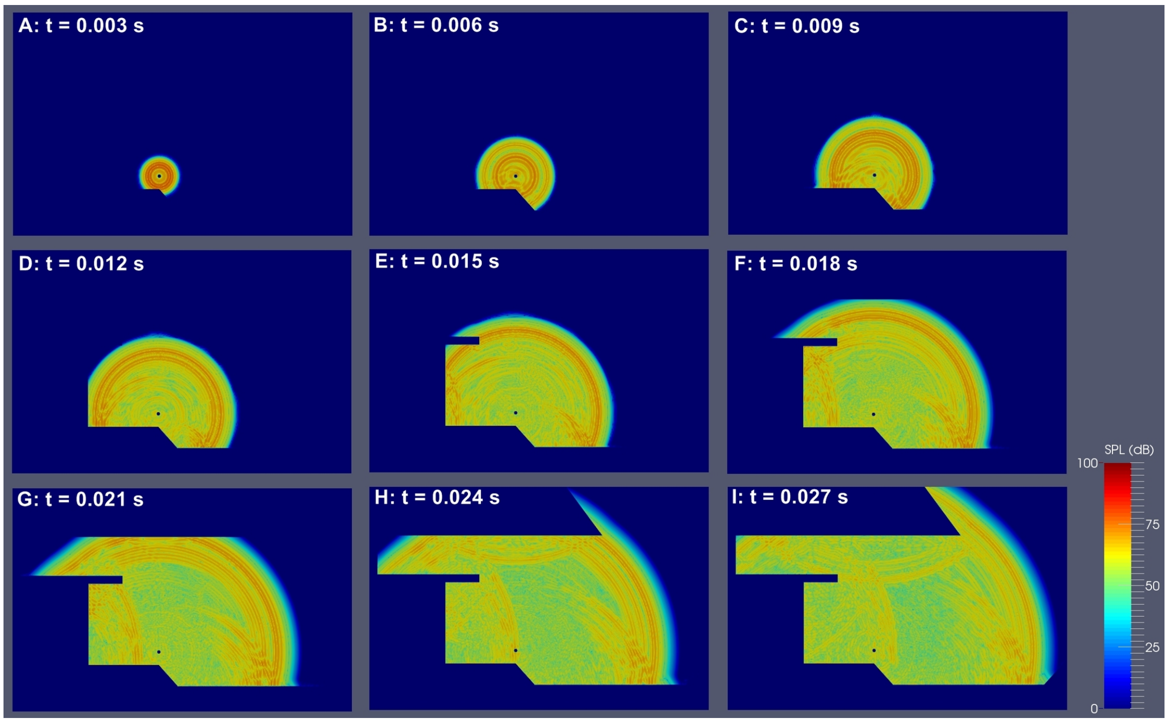

Fig. 21. Case 4: Cross section view of SPL at x_3 = -1.5 m. The constructive wave interferences of reflected waves are observed.

are multiple different Mach Cones caused by the differences of the following waves' speeds, respectively, (i) the acoustic wave and the P-wave in the pile; (ii) the acoustic wave and the S-wave in the pile; (iii) the P-wave in the sediment and the P-wave in the pile; (iv) the S-wave in the sediment and the P-wave in the pile; (v) the P-wave in the sediment and the S-wave in the pile; and (vi) the S-wave in the sediment and the S-wave in the pile. The angles of Mach Cones in our numerical results match those that are theoretically evaluated. This Mach cone wave behavior had been previously studied by Reinhall and Dahl [1] and Tsouvalas [15]. Unlike the previous work [1], this work computes the shear wave in sediment and the downward-propagating shear wave in a pile. Therefore, in lieu of 2 Mach Cones in fluid and sediment induced by a downward-propagating P-wave in a pile shown in the previous work [1], this work presented 6 Mach Cones in fluid and sediment induced by downward-propagating P- and S-waves in a pile.

It has been already shown by Reinhall and Dahl [1] that the Mach cones in fluid are accountable for intense amplitudes of underwater piling noise. However, the four elastic wave Mach Cones, shown in this paper, do not significantly contribute to the underwater noise even though they interact with the fluid above the fluid-sediment interface. Therefore, the effect of the four elastic wave Mach Cones is not noticeable in the measurement made by hydrophones so that field data can hardly provide evidence about them. On the other hand, another possible set of four elastic wave Mach Cones, induced by upward-propagating elastic waves in a pile, could noticeably affect fluid-pressure waves as suggested by Reinhall and Dahl [1]. Our simulation does not show these elastic wave Mach Cones, induced by upward-propagating elastic waves in a pile, because the pile is truncated by using a non-reflection boundary condition.

The numerical results for piles with axially-asymmetric cross-sectional shapes (Case 2) show that the close-range underwater noise for each asymmetric cross-sectional shape undergoes constructive and destructive wave interferences in contrast to the smooth radial expansion of the wave generated from an axially-symmetric pile. Therefore, the amplitudes of the close-range underwater noise are dependent on the cross-sectional geometry of a pile. Thus, engineers could optimize the cross-sectional shape (potentially axially-asymmetric) of a pile such that it will minimize 'undesired' wave energy, radiating into surrounding close-range fluid, but maximize the energy transmitted into its underlying seabed: a similar application of wave energy focusing was demonstrated by Jeong et al. [54]. The presented SEM solver could serve as a wave solver in the optimization procedure.

When axially-asymmetric surrounding solid conditions are considered (Cases 3 and 4), waves reverberate back to the fluid domain, after reaching the surface of surrounding walls. Thus, constructive and destructive interferences of waves take place, producing higher levels of underwater noise than an axially-symmetric surrounding setting. When a pile is constructed in a close-in harbor area, the reflection and diffraction waves from the surrounding solids (i.e., breakwaters, piers, and harbor walls) and sloped sediment would create constructive interference and increase the amplitudes of underwater piling noises.

In summary, the presented simulations suggest that the SEM can be an alternative method for obtaining close-range in-water pile driving noise, considering an axially-asymmetric surrounding solid condition and an axially-asymmetric pile cross-section geometry.

5. Future studies

The presented SEM study can be extended further as follows. We will compare an SEM solution to other numerical solutions of the benchmark problem in the COMPILE workshop [23]. By comparing SEM results to those by FEM models for the benchmark problem in the workshop, we could present the advantage and disadvantage of the SEM approach over the other approach. Furthermore, the SEM solution can be validated via comparison with measurement data in real piling sites given by Dahl and Dall'Osto [19], who describe the information of the field test of underwater piling in a detailed manner. Their work [19] approximately showed the geometry of an axially-asymmetric surrounding setting with a sloped sediment bathymetry. Therefore, the field data in their paper could be a good benchmark data to be compared with the 3D SEM numerical solutions. However, even their paper does not show the information of the impact force signal and the material properties of the sediment. Thus, they should be guessed in our validation study.

We should also investigate the piling noise behaviors of a shell-type hollow pile because the Mach Cone behavior around a solid pile may differ from that in a shell-type hollow pile. In the presented SEM simulations, uncertainty may be present in a number of input parameters, such as the bathymetry and material properties of sediment and a force signal. These uncertainties can affect the probabilistic distributions of wave responses. Thus, we could investigate the sensitivity of the piling noise to the uncertainties in these input parameters.

If we use a fluid-saturated poroelastic solid model (e.g., Biot's wave model), which is a more realistic model than an elastic solid as sediment, the behaviors of Mach Cones in the sediment will be even more complex than the presented results because of the existence of pore fluid in the sediment and their associated wave behaviors.

While the performance of the presented absorbing boundary condition (ABC) is satisfactory in the small domains, it would not be satisfactory if the waves were grazing in the fluid with very small angles with respect to the plane of the ABC. That is, the presented ABC in the fluid element has only a normal component of absorbing capacity with respect to the plane of the ABC so that the ABC would not be effective when the incident angle is grazing. To address this issue, we should use the perfectly-matched-layers (PML), which is known to be effective regardless of the frequency contents and incident angles of the waves. In particular, we should use the PML that is studied by Xie et al. [48] for coupled fluid-solid media.

Because it will take a large computational cost to use the SEM solution approach for computing far-range solutions for force signals with high-frequency contents, the usage of the SEM should be limited to the close-range setting (up to tens of meters distance from the piling location). Therefore, the close-range SEM numerical solution should be coupled with far-range solutions obtained by using, for instances, wavenumber integration method, or parabolic equation approximation method or normal mode expansion method.

Acknowledgment

This material is based upon work partially supported by the National Science Foundation under Award No. CMMI-1855406. Any opinions, findings, and conclusions or recommendations expressed in this material are those of the authors and do not necessarily reflect the views of the National Science Foundation.

References

1. P. G. Reinhall and P. H. Dahl, "Underwater Mach wave radiation from impact pile driving: Theory and observation," *The Journal of the Acoustical Society of America*, vol. 130, pp. 1209–1216, Sept. 2011.
2. P. T. Madsen, M. Wahlberg, J. Tougaard, K. Lucke, and P. Tyack, "Wind turbine underwater noise and marine mammals: implications of current knowledge and data needs," *Marine Ecology Progress Series*, vol. 309, pp. 279–295, Mar. 2006.
3. A. Smith, T. Stehly, and W. Musial, "2014-2015 Offshore Wind Technologies Market Report," Tech. Rep. NREL/TP-5000-64283, National Renewable Energy Laboratory, Sept. 2015.
4. I. LeProvost, "Review of Environmental Impact of the Offshore Oil and Gas Industry, Patin,

Stanislav," *Journal of Environmental Assessment Policy and Management*, vol. 3, no. 1, pp. 173–175, 2001.

5. J. Nedwell, T. Mason, R. Barham, and S. Cheesman, "Assessing the environmental impact of underwater noise during offshore windfarm construction and operation," in *Proceedings of Acoustics 2012, Fremantle, Australia 21-23 November*, 2012.
6. J. Tougaard, P. T. Madsen, and M. Wahlberg, "Underwater Noise from Construction and Operation of Offshore Wind Farms," *Bioacoustics*, vol. 17, pp. 143–146, Jan. 2008.
7. Caltrans, "Technical Guidance for Assessment and Mitigation of the Hydroacoustic Effects of Pile Driving on Fish," tech. rep., California Department of Transportation Division of Environmental Analysis, Sacramento, CA 95814, Nov. 2015.
8. M. C. Hastings and A. N. Popper, "Effects of Sound on Fish," tech. rep., California Department of Transportation, Sacramento, CA 95814, Jan. 2005.
9. R. A. Kastelein, R. Gransier, M. A. T. Marijt, and L. Hoek, "Hearing frequency thresholds of harbor porpoises (Phocoena phocoena) temporarily affected by played back offshore pile driving sounds," *The Journal of the Acoustical Society of America*, vol. 137, pp. 556–564, Feb. 2015.
10. C. Erbe, "Underwater Noise from Pile Driving in Moreton Bay, QLD," *Acoustics Australia*, vol. 37, pp. 87–92, Dec. 2009.
11. P. H. Dahl, C. A. F. de Jong, and A. N. Popper, "The Underwater Sound Field from Impact Pile Driving and Its Potential Effects on Marine Life," *Journal of Acoustical Society of America*, vol. 11, no. 2, 2015.
12. R. A. Kastelein, D. van Heerden, R. Gransier, and L. Hoek, "Behavioral responses of a harbor porpoise (Phocoena phocoena) to playbacks of broadband pile driving sounds," *Marine Environmental Research*, vol. 92, pp. 206–214, Dec. 2013.
13. A. Tsouvalas and A. V. Metrikine, "Noise reduction by the application of an air-bubble curtain in offshore pile driving," *Journal of Sound and Vibration*, vol. 371, pp. 150–170, June 2016.
14. A. Tsouvalas and A. V. Metrikine, "A semi-analytical model for the prediction of underwater noise from offshore pile driving," *Journal of Sound and Vibration*, vol. 332, pp. 3232–3257, June 2013.
15. A. Tsouvalas and A. V. Metrikine, "A Three-Dimensional Semi-analytical Model for the Prediction of Underwater Noise Generated by Offshore Pile Driving," in *Fluid-Structure-Sound Interactions and Control* (Y. Zhou, Y. Liu, L. Huang, and D. H. Hodges, eds.), Lecture Notes in Mechanical Engineering, pp. 259–264, Springer Berlin Heidelberg, 2014. DOI: 10.1007/978-3-642-40371-2_38.
16. A. Tsouvalas, *Underwater Noise Generated by Offshore Pile Driving*. Dissertation, Delft University of Technology, The Netherlands, Nov. 2015.
17. A. Tsouvalas and A. Metrikine, "Parametric study of noise reduction by an air-bubble curtain in offshore pile driving," *ICSV 2016 - 23rd International Congress on Sound and Vibration: From Ancient to Modern Acoustics*, 2017.
18. E. E. Seylabi, C. Jeong, and E. Taciroglu, "On numerical computation of impedance functions for rigid soil-structure interfaces embedded in heterogeneous half-spaces," *Computers and Geotechnics*, vol. 72, pp. 15–27, 2016.
19. P. H. Dahl and D. R. Dall'Osto, "On the underwater sound field from impact pile driving: Arrival structure, precursor arrivals, and energy streamlines," *The Journal of the Acoustical Society of America*, vol. 142, pp. 1141–1155, Aug. 2017.
20. K. Heitmann, T. Lippert, M. Ruhnau, S. Lippert, and O. v. Estorff, "Computational prediction of the underwater sound pressure due to offshore pile driving," Institute of Modelling and Computation, Hamburg University of Technology, 21073 Hamburg, Germany, July 2014.
21. S. Lippert, T. Lippert, K. Heitmann, and O. Von Estorff, "Prediction of underwater noise and far field propagation due to pile driving for offshore wind farms," *Proceedings of Meetings on*

Acoustics, vol. 19, p. 070036, May 2013.

22. M. B. Fricke and R. Rolfes, “Towards a complete physically based forecast model for underwater noise related to impact pile driving,” *The Journal of the Acoustical Society of America*, vol. 137, pp. 1564–1575, Mar. 2015.
23. S. Lippert, M. Nijhof, T. Lippert, D. Wilkes, A. Gavrilov, K. Heitmann, M. Ruhnau, O. von Estorff, A. Schafke, I. Schafer, J. Ehrlich, A. MacGillivray, J. Park, W. Seong, M. A. Ainslie, C. de Jong, M. Wood, L. Wang, and P. Theobald, “COMPILE A Generic Benchmark Case for Predictions of Marine Pile-Driving Noise,” *IEEE Journal of Oceanic Engineering*, vol. 41, pp. 1061–1071, Oct. 2016.
24. S. Lloyd, C. Jeong, H. Nath Gharti, J. Vignola, and J. Tromp, “Spectral-element simulations of acoustic waves induced by a moving underwater source,” *Journal of Theoretical and Computational Acoustics (in press)*, 2019.
25. D. Komatitsch and J. Tromp, “Introduction to the spectral element method for three-dimensional seismic wave propagation,” *Geophysical Journal International*, vol. 139, no. 3, pp. 806–822, 1999.
26. D. Komatitsch and J. Tromp, “A perfectly matched layer absorbing boundary condition for the second-order seismic wave equation,” *Geophysical Journal International*, vol. 154, no. 1, pp. 146–153, 2003.
27. S.-J. Lee, Y.-C. Chan, D. Komatitsch, B.-S. Huang, and J. Tromp, “Effects of realistic surface topography on seismic ground motion in the Yangminshan region of Taiwan based upon the spectral-element method and LiDAR DTM,” *Bulletin of the Seismological Society of America*, vol. 99, no. 2A, pp. 681–693, 2009.
28. D. Komatitsch, C. Barnes, and J. Tromp, “Wave propagation near a fluid-solid interface: A spectral-element approach,” *Geophysics*, vol. 65, no. 2, pp. 623–631, 2000.
29. D. Komatitsch, J. Ritsema, and J. Tromp, “The spectral-element method, Beowulf computing, and global seismology,” *Science*, vol. 298, no. 5599, pp. 1737–1742, 2002.
30. D. Komatitsch, R. Martin, J. Tromp, M. A. Taylor, and B. A. Wingate, “Wave propagation in 2-D elastic media using a spectral element method with triangles and quadrangles,” *Journal of Computational Acoustics*, vol. 9, no. 02, pp. 703–718, 2001.
31. D. Komatitsch, S. Tsuboi, and J. Tromp, “The spectral-element method in seismology,” *Seismic Earth: Array Analysis of Broadband Seismograms*, pp. 205–227, 2005.
32. D. Komatitsch, Q. Liu, J. Tromp, P. Süss, C. Stidham, and J. H. Shaw, “Simulations of ground motion in the Los Angeles basin based upon the spectral-element method,” *Bulletin of the Seismological Society of America*, vol. 94, no. 1, pp. 187–206, 2004.
33. C. Morency and J. Tromp, “Spectral-element simulations of wave propagation in porous media,” *Geophysical Journal International*, vol. 175, no. 1, pp. 301–345, 2008.
34. J. Tromp, D. Komattisch, and Q. Liu, “Spectral-element and adjoint methods in seismology,” *Communications in Computational Physics*, vol. 3, no. 1, pp. 1–32, 2008.
35. R. Stephen, I. Udovydchenkov, S. Bolmer, D. Komatitsch, J. Tromp, E. Casarotti, Z. Xie, and P. Worcester, “Three dimensional numerical modeling of bottom-diffracted surface-reflected arrivals in the North Pacific.,” in *Fall AGU meeting, San Francisco, December 14-18*, 2015.
36. D. Peter, D. Komatitsch, Y. Luo, R. Martin, N. Le Goff, E. Casarotti, P. Le Loher, F. Magnoni, Q. Liu, C. Blitz, T. Nissen-Meyer, P. Basini, and J. Tromp, “Forward and adjoint simulations of seismic wave propagation on fully unstructured hexahedral meshes,” *Geophysical Journal International*, vol. 186, pp. 721–739, Aug. 2011.
37. Z. Xie, R. Matzen, P. Cristini, D. Komatitsch, and R. Martin, “A perfectly matched layer for fluid-solid problems: Application to ocean-acoustics simulations with solid ocean bottoms,” *The Journal of the Acoustical Society of America*, vol. 140, no. 1, pp. 165–175, 2016.
38. D. Komatitsch and J. Tromp, “Spectral-element simulations of global seismic wave propagation

– I. Validation," *Geophysical Journal International*, vol. 149, pp. 390–412, 2002.
39. J. Tromp, D. Komatitsch, V. Hjrleifsdttir, Q. Liu, H. Zhu, D. Peter, E. Bozdag, D. McRitchie, P. Friberg, C. Trabant, and A. Hutko, "Near real-time simulations of global cmt earthquakes," *Geophysical Journal International*, vol. 183, no. 1, pp. 381–389, 2010.
40. C. Jeong, S.-W. Na, and L. F. Kallivokas, "Near-surface localization and shape identification of a scatterer embedded in a halfplane using scalar waves," *Journal of Computational Acoustics*, vol. 17, no. 03, pp. 277–308, 2009.
41. J. W. Kang and L. F. Kallivokas, "The inverse medium problem in heterogeneous PML-truncated domains using scalar probing waves," *Computer Methods in Applied Mechanics and Engineering*, vol. 200, no. 1, pp. 265–283, 2011.
42. L. F. Kallivokas, A. Fathi, S. Kucukcoban, K. H. Stokoe, J. Bielak, and O. Ghattas, "Site characterization using full waveform inversion," *Soil Dynamics and Earthquake Engineering*, vol. 47, pp. 62–82, 2013.
43. J. Jung and E. Taciroglu, "Modeling and identification of an arbitrarily shaped scatterer using dynamic XFEM with cubic splines," *Computer Methods in Applied Mechanics and Engineering*, vol. 278, pp. 101–118, 2014.
44. R. Stacey, "Improved transparent boundary formulations for the elastic-wave equation," *Bulletin of the Seismological Society of America*, vol. 78, no. 6, pp. 2089–2097, 1988.
45. A. Quarteroni, A. Tagliani, and E. Zampieri, "Generalized galerkin approximations of elastic waves with absorbing boundary conditions," *Computer Methods in Applied Mechanics and Engineering*, vol. 163, no. 1-4, pp. 323–341, 1998.
46. D. Komatitsch, S. Tsuboi, and J. Tromp, "The spectral-element method in seismology," in *Geophysical Monograph Series* (A. Levander and G. Nolet, eds.), vol. 157, pp. 205–227, Washington, D. C.: American Geophysical Union, 2005.
47. P. Cristini and D. Komatitsch, "Some illustrative examples of the use of a spectral-element method in ocean acoustics," *The Journal of the Acoustical Society of America*, vol. 131, pp. EL229–EL235, Mar. 2012.
48. Z. Xie, R. Matzen, P. Cristini, D. Komatitsch, and R. Martin, "A perfectly matched layer for fluid-solid problems: Application to ocean-acoustics simulations with solid ocean bottoms," *The Journal of the Acoustical Society of America*, vol. 140, no. 1, pp. 165–175, 2016.
49. H. Bao, J. Bielak, O. Ghattas, L. F. Kallivokas, D. R. O'Hallaron, J. R. Shewchuk, and J. Xu, "Large-scale simulation of elastic wave propagation in heterogeneous media on parallel computers," *Computer Methods in Applied Mechanics and Engineering*, vol. 152, no. 1, pp. 85–102, 1998.
50. R. Courant, K. Friedrichs, and H. Lewy, "Uber die partiellen Differenzengleichungen der mathematischen Physik | SpringerLink," *Mathematische Annalen*, vol. 100, pp. 32–74, 1928.
51. G. Mavko, T. Mukerji, and J. Dvorkin, *The Rock Physics Handbook, Second Edition.* New York: Cambridge University Press, 2012.
52. A. Gholamy and V. Kreinovich, *Why Ricker Wavelets Are Successful in Processing Seismic Data: Towards a Theoretical Explanation.* PhD thesis, University of Texas at El Paso, 00 W. University El Paso, TX 79968, USA.
53. Y. H. Lee and T. Oh, "The measurement of P-, S-, and R-wave velocities to evaluate the condition of reinforced and prestressed concrete slabs," *Advances in Materials Science and Engineering*, vol. 2016, p. Article ID 1548215, 2016.
54. C. Jeong, L. Kallivokas, S. Kucukcoban, W. Deng, and A. Fathi, "Maximization of wave motion within a hydrocarbon reservoir for wave-based enhanced oil recovery," *Journal of Petroleum Science and Engineering*, vol. 129, pp. 205–220, 2015.
55. M. Zampolli, M. J. J. Nijhof, C. A. F. de Jong, M. A. Ainslie, E. H. W. Jansen, and B. A. J. Quesson, "Validation of finite element computations for the quantitative prediction of underwa-

ter noise from impact pile driving," *The Journal of the Acoustical Society of America*, vol. 133, pp. 72–81, Jan. 2013.